

# Supplemental Material: Dispersive Dark Excitons in van der Waals Ferromagnet CrI<sub>3</sub>

(Dated: January 1, 2025)

This document provides a resonant inelastic x-ray scattering (RIXS) energy map measured with linear vertical ( $\sigma$ ) polarization, x-ray absorption spectroscopy (XAS) data, additional temperature dependence of RIXS spectra measured at  $E_{e_g}$  resonance, detailed description of the fitting procedures for the RIXS data with linecuts showing the fitting, plots showing integrated peak intensity temperature dependence, further details of our exact diagonalization (ED) calculations, and a discussion of terminology for the excitations studies here.

## S1. ADDITIONAL RIXS ENERGY MAP WITH $\sigma$ POLARIZATION AND XAS DATA

Besides the incident energy dependent RIXS intensity map measured with linear horizontal ( $\pi$ ) polarization shown in the main text, we also collected data with linear vertical ( $\sigma$ ) polarization as displayed in Fig. S1. All experimental parameters were kept the same for these two sets of measurements, with the only difference being the incident x-ray polarization. The two RIXS energy maps are very similar with nearly identical resonance behaviors, although the  $\sigma$ -channel data has slightly lower intensity. We therefore chose  $\pi$ -polarization for the following angular and temperature-dependent measurements to maximize the RIXS intensity. The XAS also exhibits a weak dichroism for the two polarizations, as shown in Fig. S2.

## S2. ADDITIONAL TEMPERATURE DEPENDENCE OF RIXS SPECTRA AT $E_{e_g}$ RESONANCE

Besides the temperature dependent RIXS intensity map measured at  $E_{t_{2g}}$  resonance shown in the main text, we also have data collected at  $E_{e_g}$  resonance as displayed in Fig. S3. As described in detail in the next section, we co-fit these two data sets with shared exciton widths and energies. Just like the data at  $E_{t_{2g}}$ , the excitons also exhibit abrupt changes in peak height near the ferromagnetic (FM) transition temperature  $T_c$  at this resonance, although the changes are less dramatic.

## S3. FITTING OF THE RIXS SPECTRA

### A. Functional form

We fit RIXS spectra with five peaks plus a linear background to parameterize the excitons as a function of incident energy, momentum transfer, or temperatures. We used Voigt functions to fit the dark excitons D1–D2 and bright excitons B2–B3. The width of the Gaussian component was fixed to the energy resolution of 30.5 meV, which was determined by a reference measurement on a multilayer heterostructure sample with a strong elastic scattering signal. The bright exciton B1 is better described by a Gaussian lineshape. We found that these simple lineshapes provide a satisfactory fit to the spectra.

To obtain high-precision values for the exciton energies, we carefully calibrated the energy zero of the spectra. In the low-energy region of the spectra, we identified one prominent elastic peak along with a weak magnon feature in the tail of peak. We used a Gaussian function with its width fixed to the energy resolution to fit the elastic peak. For the magnon, we chose a damped harmonic oscillator (DHO) function below and convoluted this function with a Gaussian resolution function to model it. The form of the DHO function we used is:

$$S(\mathbf{Q}, \omega) = \frac{\omega \chi_Q}{1 - \exp(-\omega/k_B T)} \cdot \frac{2z_Q f_Q}{(\omega^2 - f_Q^2)^2 + (\omega z_Q)^2} \quad (1)$$

where  $f_Q$  is the undamped energy,  $\chi_Q$  is the oscillator strength,  $z_Q$  is the damping factor,  $k_B$  is the Boltzmann constant, and  $T$  is temperature. Because the elastic peak dominates the spectral weight in this region, the inclusion of the magnon peak in the fitting function has minimal effect on the fitted elastic peak position. The error bars for the fitted exciton peak positions shown in Fig. 2 include not only their own fitting errors but also the fitting errors of the energy zero.

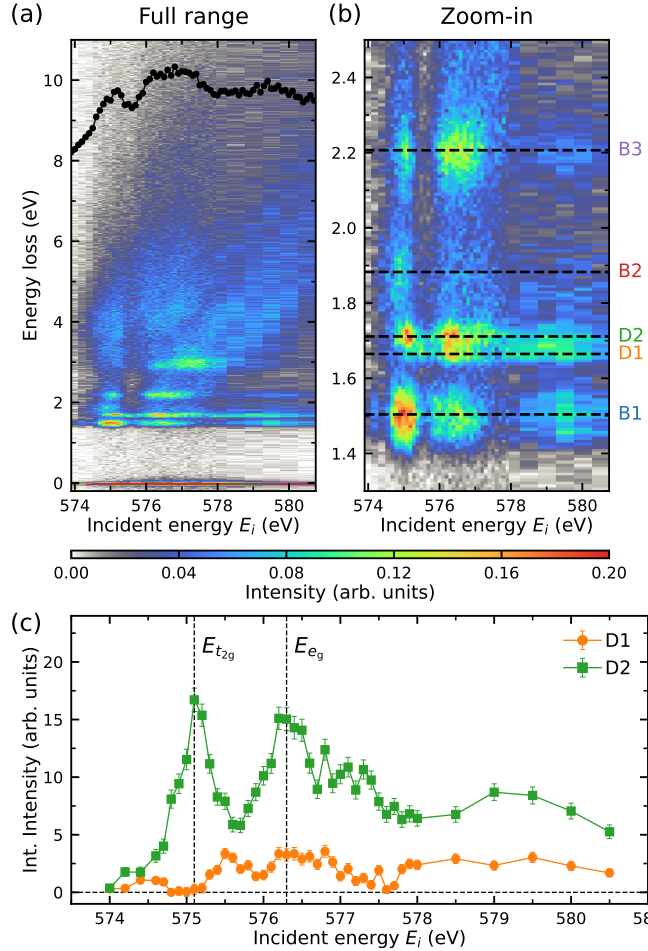


FIG. S1. Additional resonance behavior of dark excitons measured with linear vertical ( $\sigma$ ) polarization. (a) Incident photon energy  $E_i$  dependence of the RIXS intensity map at the Cr  $L_3$ -edge with  $\sigma$ -polarized incident x-rays. The measurement was taken at  $T = 30$  K with x-rays incident on the sample at  $\theta = 14.5^\circ$  and scattered to  $2\Theta = 150^\circ$  in the  $(H0L)$  scattering plane. The overlaid black curve on the top is XAS spectrum taken at the same conditions (including x-ray polarization, experimental geometry, and temperature). (b) Zoom-in of the RIXS energy map in the vicinity of the dark excitons. Horizontal dashed lines are fitted exciton energies. (c) The fitted integrated intensities of the two dark excitons as a function of incident photon energy  $E_i$ . Error bars represent one standard deviation. Similar to the  $\pi$  polarization data in the main text, both dark excitons reach their local maxima in intensity at  $E_{e_g}$ , while D1 has nearly zero spectral weight at  $E_{t_{2g}}$ .

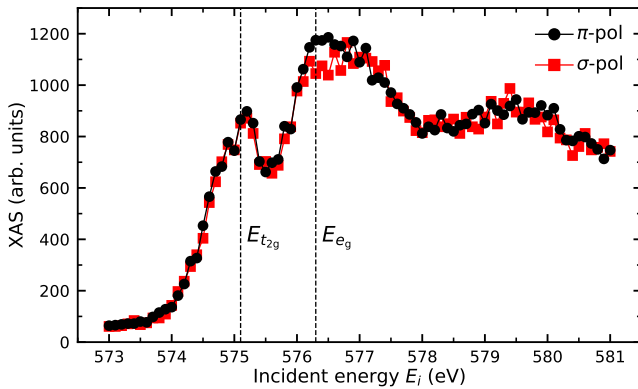


FIG. S2. XAS spectra with both linear horizontal ( $\pi$ ) and linear vertical ( $\sigma$ ) polarizations. The spectra were taken at  $T = 30$  K. The sample geometry was the same as the measurement for the RIXS energy map (i.e.,  $\theta = 14.5^\circ$ ,  $2\Theta = 150^\circ$ ,  $(H0L)$  scattering plane) but with a much larger exit slit size of 300  $\mu\text{m}$ . The vertical dashed lines label the two resonant energies. This is the same data shown in Figs. 1 and S1 and provided here to show the comparison between the two polarizations.

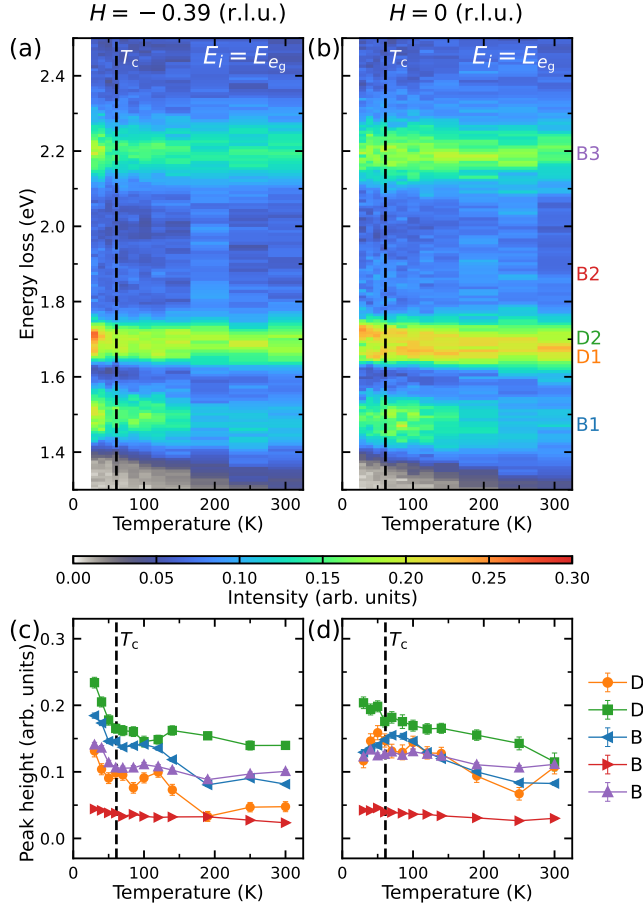


FIG. S3. Additional temperature dependence of the dark excitons at  $E_{eg}$  resonance. (a),(b) RIXS intensity map as a function of temperature measured at two different in-plane momenta ( $H = -0.39$  and  $H = 0$  r.l.u., respectively) with the same incident energy  $E_{eg}$ . (c),(d) Corresponding peak height extracted from the fits as a function of temperature. Error bars represent one standard deviation. The dashed lines indicate the FM transition temperature  $T_c$ .

### B. Incident energy dependence

As expected for a Raman-like RIXS process, the exciton energies and widths were found to be independent of incident energy, providing additional constraints in fitting the incident energy dependent RIXS spectra. Specifically, we first co-fitted all the spectra taken with  $\pi$ -polarization, applying the constraints that each exciton maintains the same position and width across all spectra (see Fig. S4). Then, we co-fitted all the spectra taken with  $\sigma$ -polarization. As shown in Fig. S5, we found that even when we forced the exciton positions and widths to match the fitted values obtained from the  $\pi$ -polarization data, the fits still look reasonably good, demonstrating the robustness of the fitting result.

### C. In-plane momentum transfer dependence

For the fitting of the RIXS spectra at various in-plane momentum transfers, since we have measurements at two incident energies, we applied the above-mentioned co-fitting method and constrained the exciton energy and widths to be the same across both spectra. Such a co-fitting strategy with shared exciton positions and widths is particularly useful in obtaining consistent fits for the dark exciton D1, which has a minuscule spectral weight at  $E_{t_{2g}}$  resonance. We present the best fits to the linecuts of the RIXS spectra in Fig. S6–S8. In Fig. S9, we show the fitted peak positions of the three bright excitons as a function of the in-plane momentum transfers. No clear dispersion is detected for these excitons beyond their error bars.

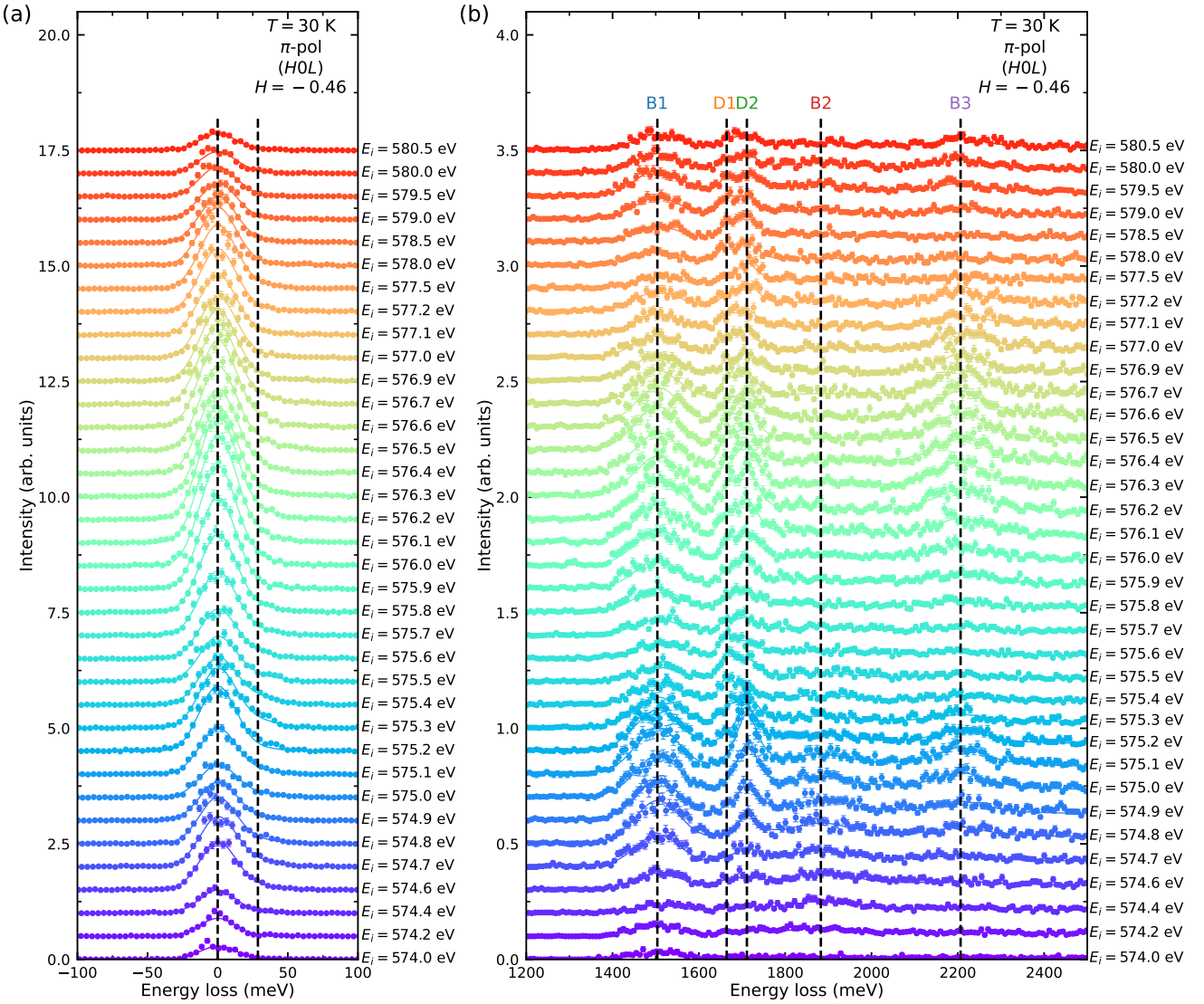


FIG. S4. RIXS spectra measured at various incident energies with linear-horizontally ( $\pi$ -) polarized x-rays. (a) RIXS spectra near the elastic line. (b) RIXS spectra in the energy window covering the excitons. The measurements were taken at various incident photon energy through the Cr  $L_3$ -edge measured in the ( $HOL$ ) plane at  $T = 30\text{ K}$ . These data are the same as the intensity maps shown in Fig. 1(a)–(b) and are provided to show the linecuts directly. Data are shifted vertically for clarity. The solid lines are the fits to the data. Error bars represent one standard deviation. Vertical black dashed lines label the exciton energies.

#### D. Temperature dependence

We used the same co-fitting approach to fit the temperature-dependent RIXS spectra. However, due to the broadening of the exciton peaks, not every spectrum yielded a converged fitting result. Therefore, we added additional constraints, including the integrated intensity of B2 at both resonance energies and the integrated intensity of D1 at the  $E_{t_{2g}}$  resonance. We found that these quantities have minimal temperature dependence, so we fixed them to their respective average values obtained from the initial fits. The final best fits to the temperature-dependent RIXS spectra are shown in Fig. S10 and S11. Figure S12 displays the fitted peak positions of all five excitons as a function of temperature measured. B1 (and to a lesser extent D2) shows a clear red-shift upon warming. The red shift is less apparent for other excitons, partly due to their weak intensities and/or broad peak width.

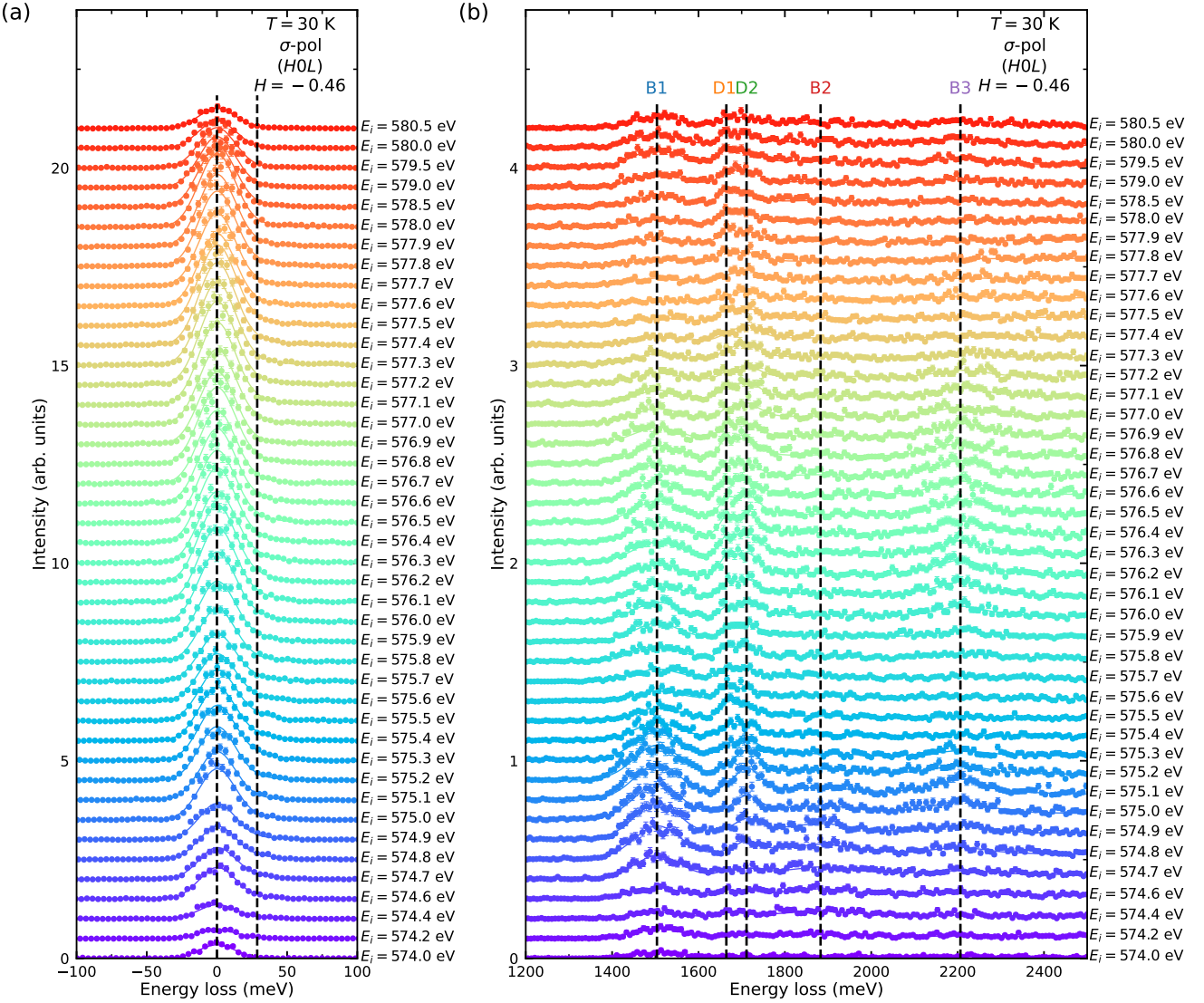


FIG. S5. RIXS spectra measured at various incident energies with linear-vertically ( $\sigma$ -) polarized x-rays. (a) RIXS spectra near the elastic line. (b) RIXS spectra in the energy window covering the excitons. The measurements were taken at various incident photon energy through the Cr  $L_3$ -edge measured in the ( $HOL$ ) plane at  $T = 30 \text{ K}$ . These data are the same as the intensity maps shown in Fig. S1(a)–(b) and are provided to show the linecuts directly. Data are shifted vertically for clarity. The solid lines are the fits to the data. Error bars represent one standard deviation. Vertical black dashed lines label the exciton energies.

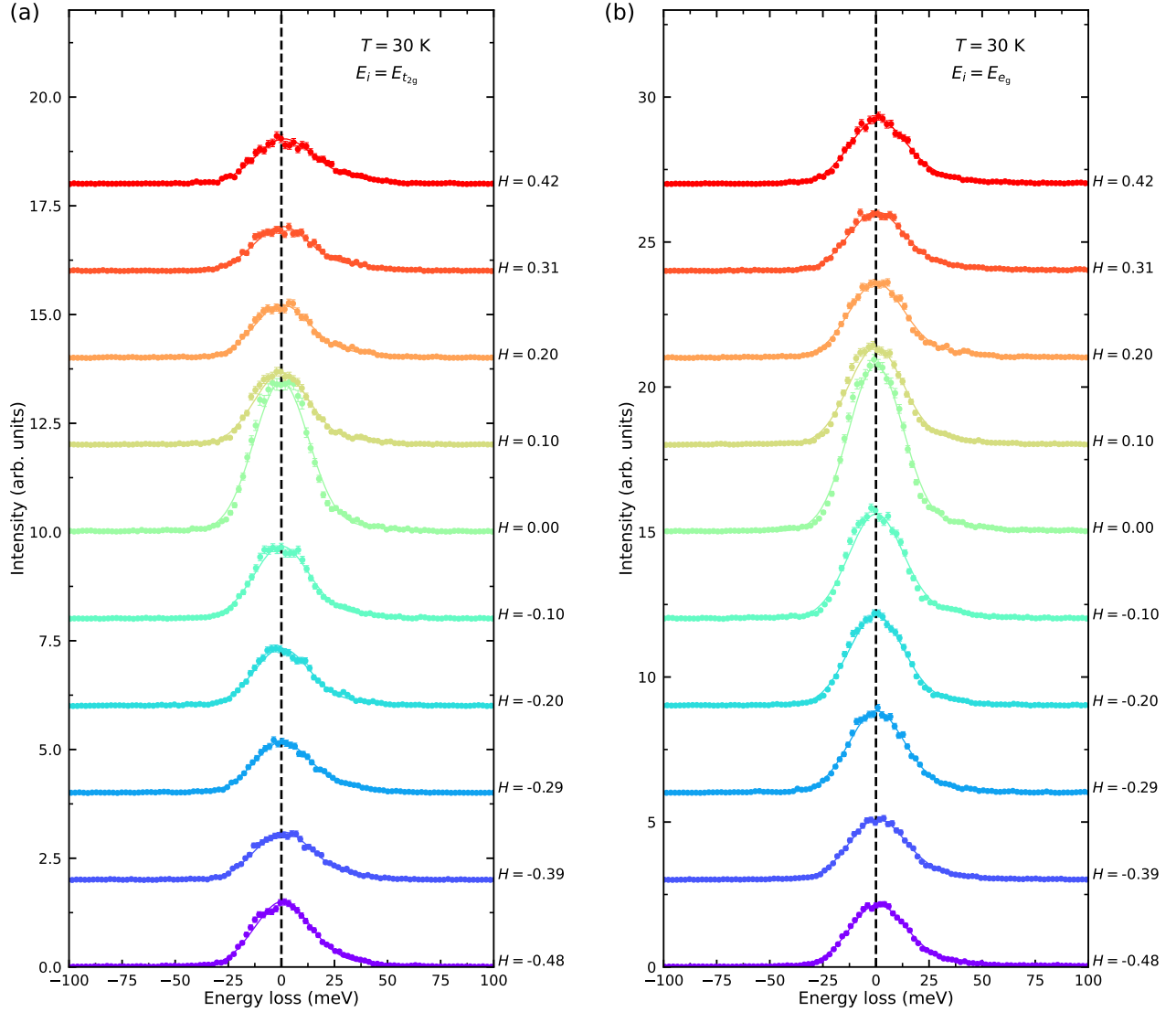


FIG. S6. RIXS spectra measured at various in-plane momentum transfer  $H$  with an energy window chosen to isolate the elastic line. (a) RIXS spectra at  $E_{t_{2g}}$  resonance. (b) RIXS spectra at  $E_{e_g}$  resonance. The measurements were taken in the ( $H0L$ ) plane at  $T = 30 \text{ K}$  with linear horizontal ( $\pi$ ) polarization of the incident x-rays. Data are shifted vertically for clarity. The solid lines are the fits to the data. Error bars represent one standard deviation. Vertical black dashed lines label the energy zero.

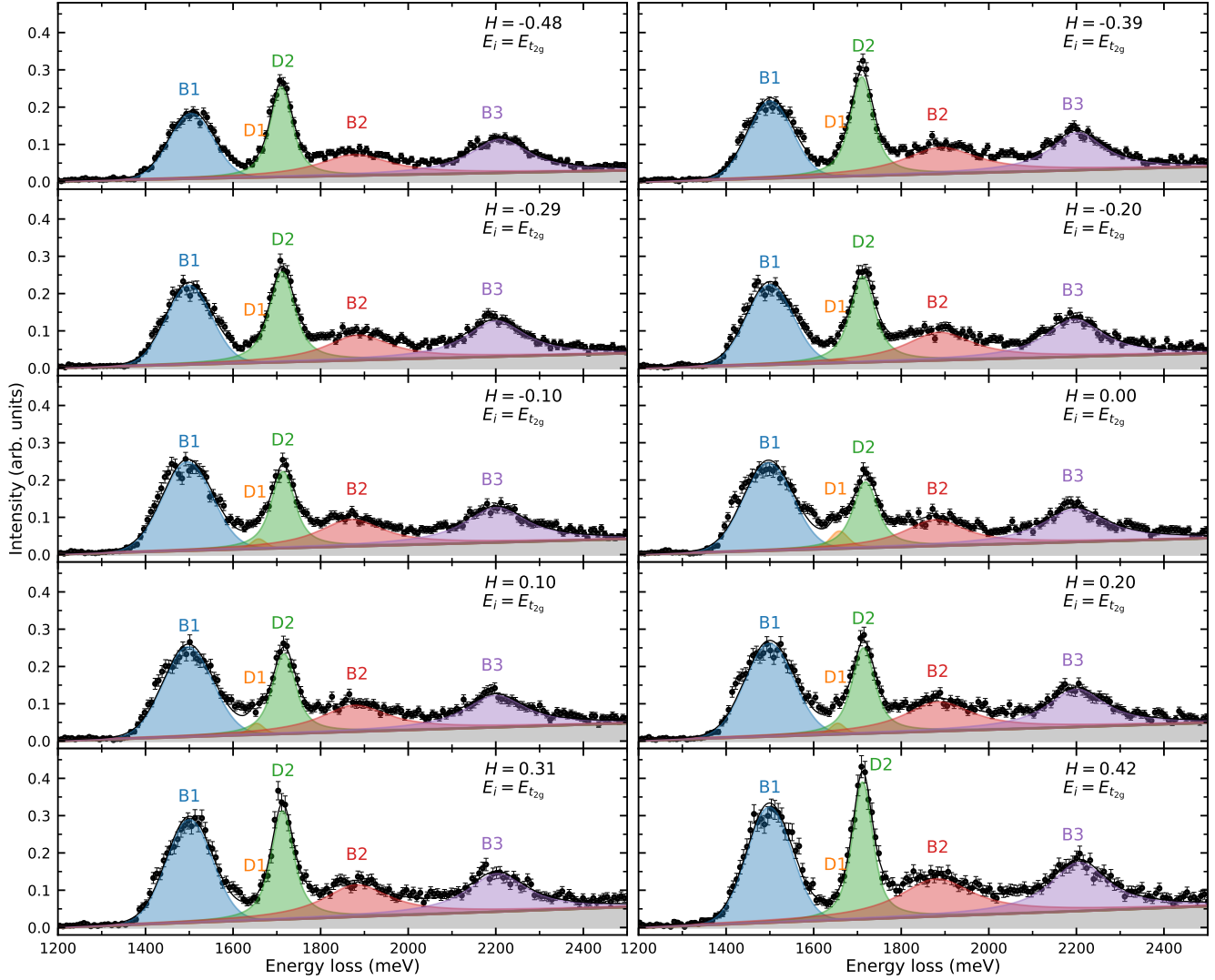


FIG. S7. RIXS spectra measured at various in-plane momentum transfer  $H$  at  $E_{t_{2g}}$  resonance with an energy window chosen to isolate the excitons. The measurements were taken in the ( $H0L$ ) plane at  $T = 30$  K with linear horizontal ( $\pi$ ) polarization of the incident x-rays. These data are the same as the intensity maps shown in Fig. 2(a) and are provided to show the linecuts directly. Solid black lines are the fits to the data, with shaded areas showing the contributions from different components. Error bars represent one standard deviation.

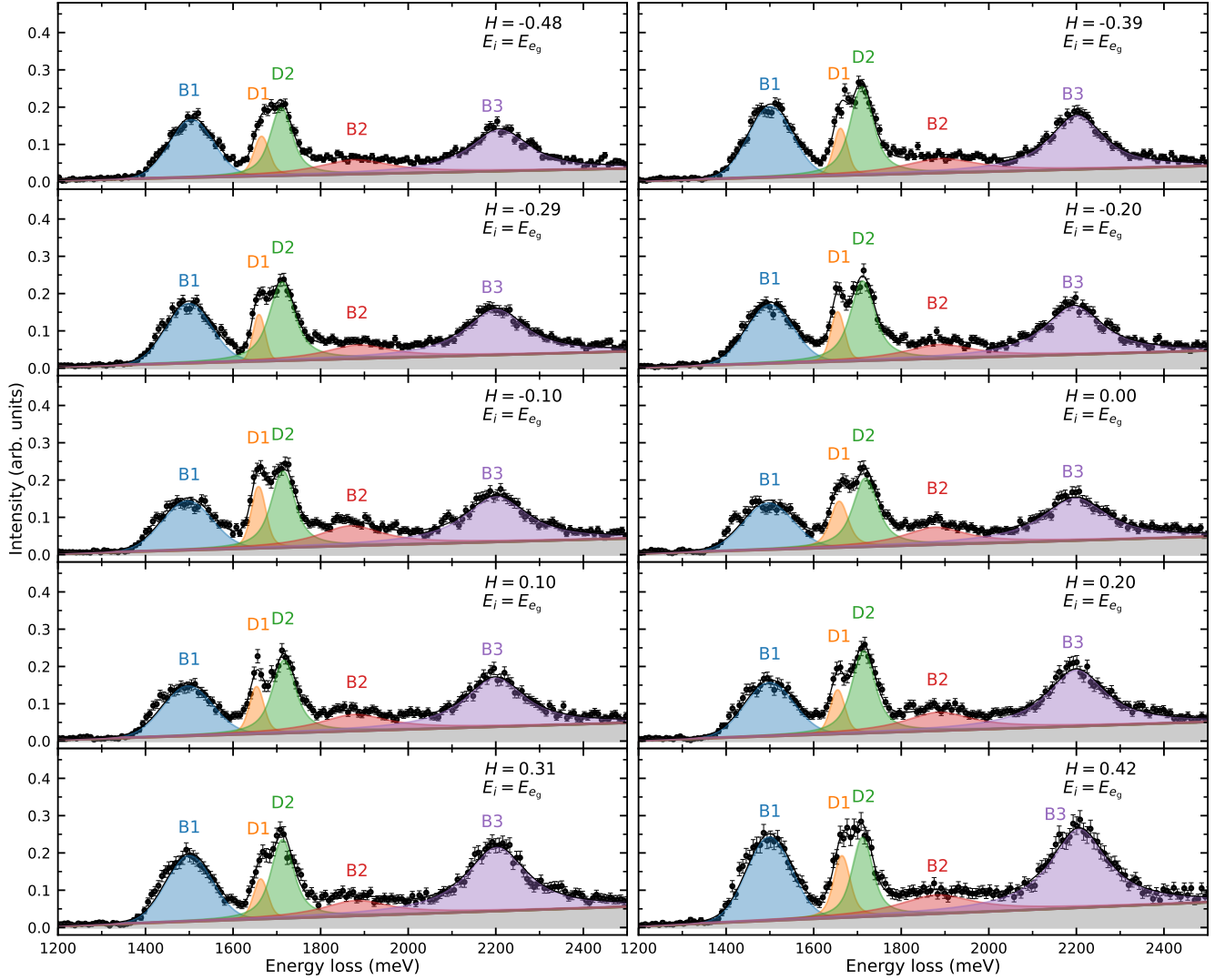


FIG. S8. RIXS spectra measured at various in-plane momentum transfer  $H$  at  $E_{eg}$  resonance with an energy window chosen to isolate the excitons. The measurements were taken in the ( $H0L$ ) plane at  $T = 30$  K with linear horizontal ( $\pi$ ) polarization of the incident x-rays. These data are the same as the intensity maps shown in Fig. 2(b) and are provided to show the linecuts directly. Solid black lines are the fits to the data, with shaded areas showing the contributions from different components. Error bars represent one standard deviation.

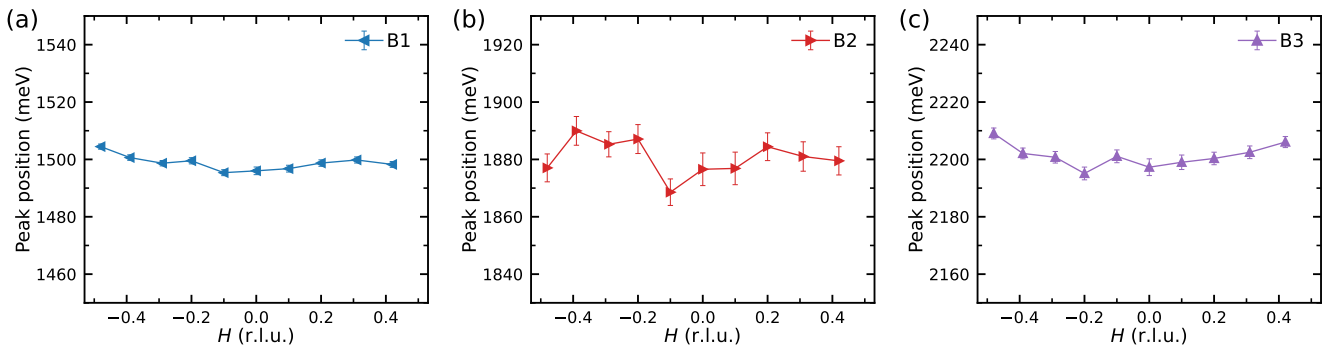


FIG. S9. The extracted momentum dependent energies of the three bright excitons. Error bars represent one standard deviation. No clear dispersion is detected for these bright excitons.

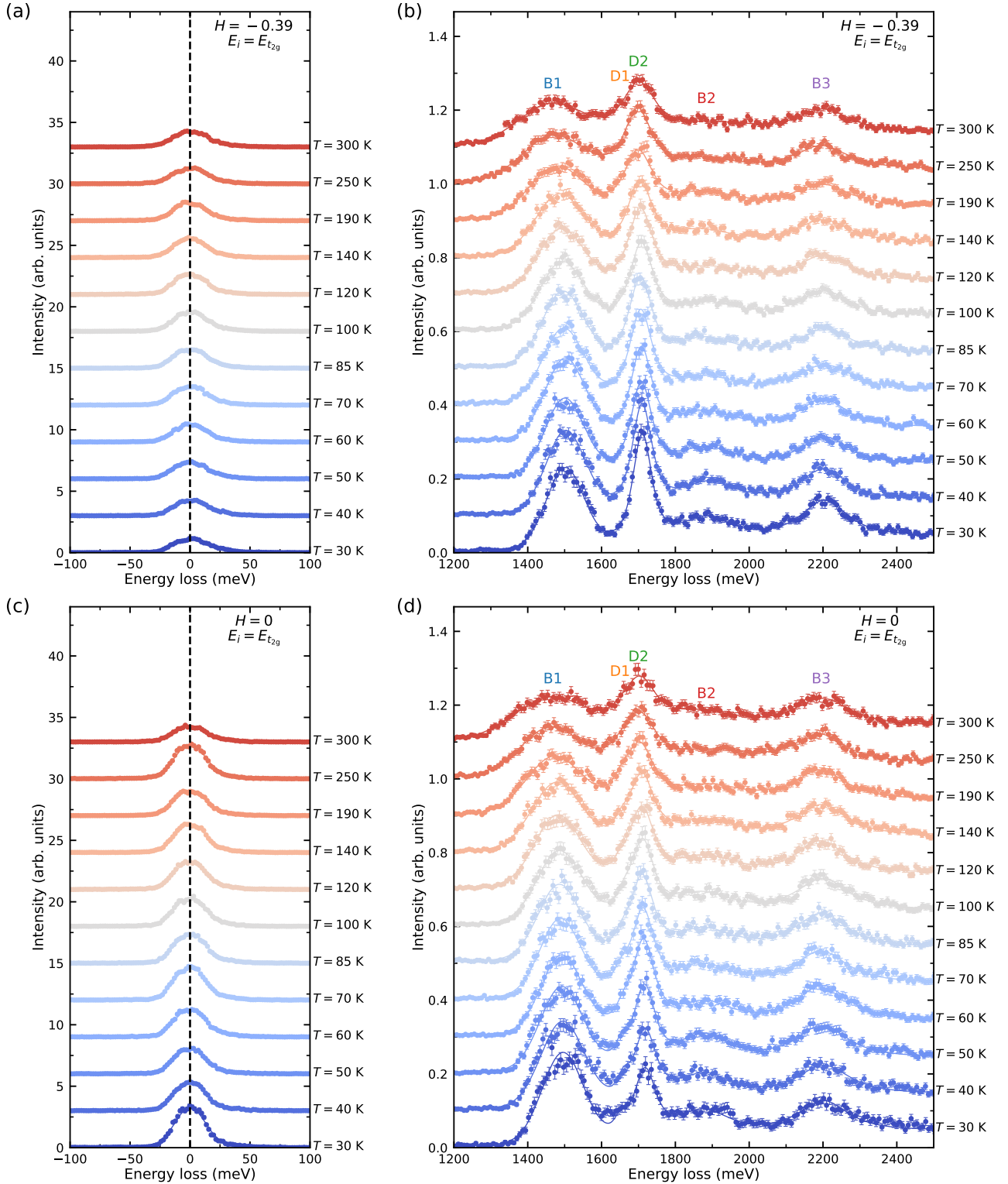


FIG. S10. RIXS spectra measured at various temperatures at  $E_{t_{2g}}$  resonance. (a),(b) RIXS spectra taken at  $H = -0.39$  r.l.u. with the energy window chosen to isolate the elastic line and excitons, respectively. (c),(d) RIXS spectra taken at  $H = 0$  r.l.u. with the energy window chosen to isolate the elastic line and excitons, respectively. All the measurements were done with linear horizontal ( $\pi$ ) polarization of the incident x-rays. These data are the same as the intensity maps shown in Fig. 3(a)–(b) and are provided to show the linecuts directly. Data are shifted vertically for clarity. The solid lines are the fits to the data. Error bars represent one standard deviation. Vertical dashed lines label the energy zero.

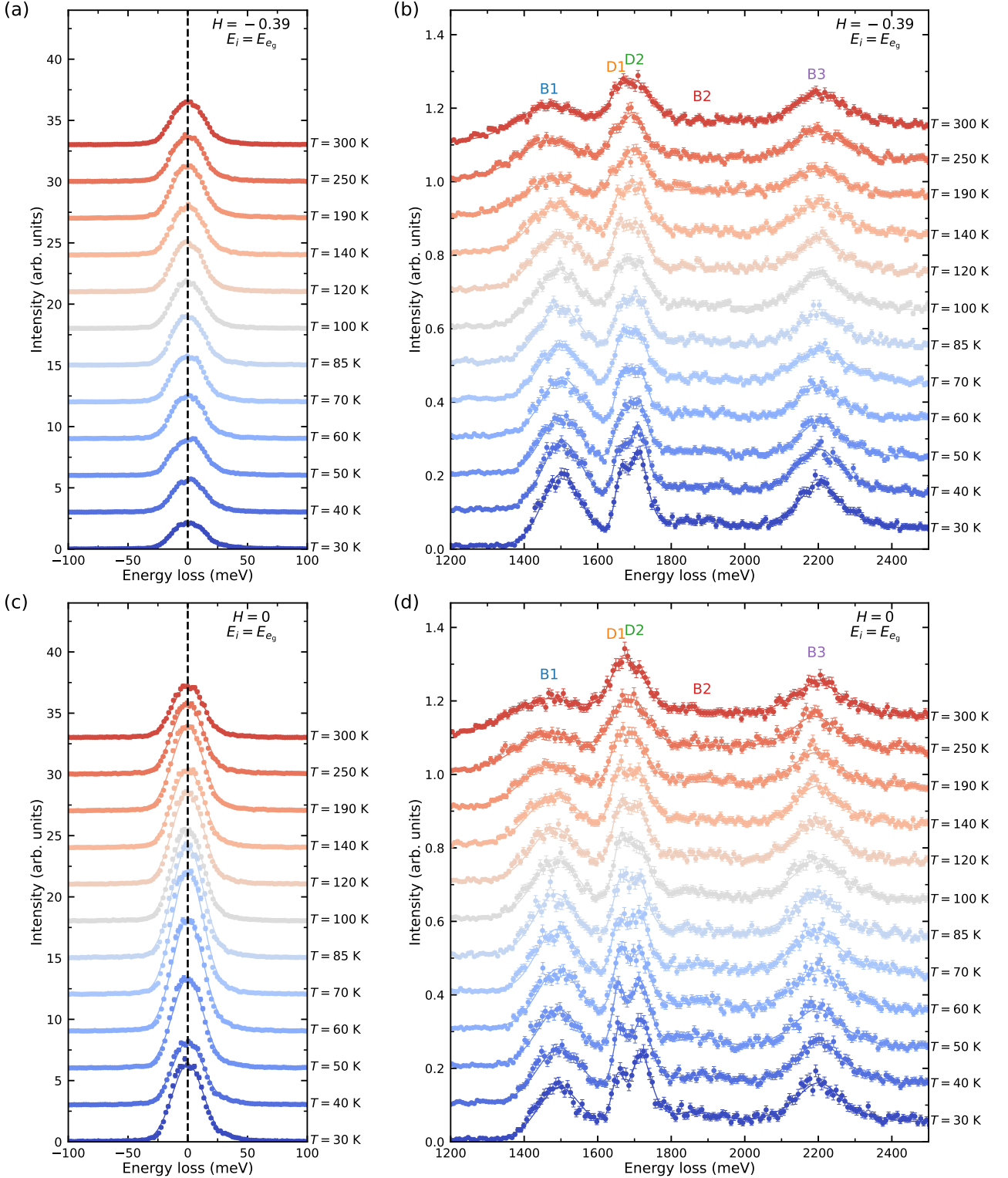


FIG. S11. RIXS spectra measured at various temperatures at  $E_{e_g}$  resonance. (a),(b) RIXS spectra taken at  $H = -0.39$  r.l.u. with the energy window chosen to isolate the elastic line and excitons, respectively. (c),(d) RIXS spectra taken at  $H = 0$  r.l.u. with the energy window chosen to isolate the elastic line and excitons, respectively. All the measurements were done with linear horizontal ( $\pi$ ) polarization of the incident x-rays. These data are the same as the intensity maps shown in Fig. S3(a)–(b) and are provided to show the linecuts directly. Data are shifted vertically for clarity. The solid lines are the fits to the data. Error bars represent one standard deviation. Vertical dashed lines label the energy zero.

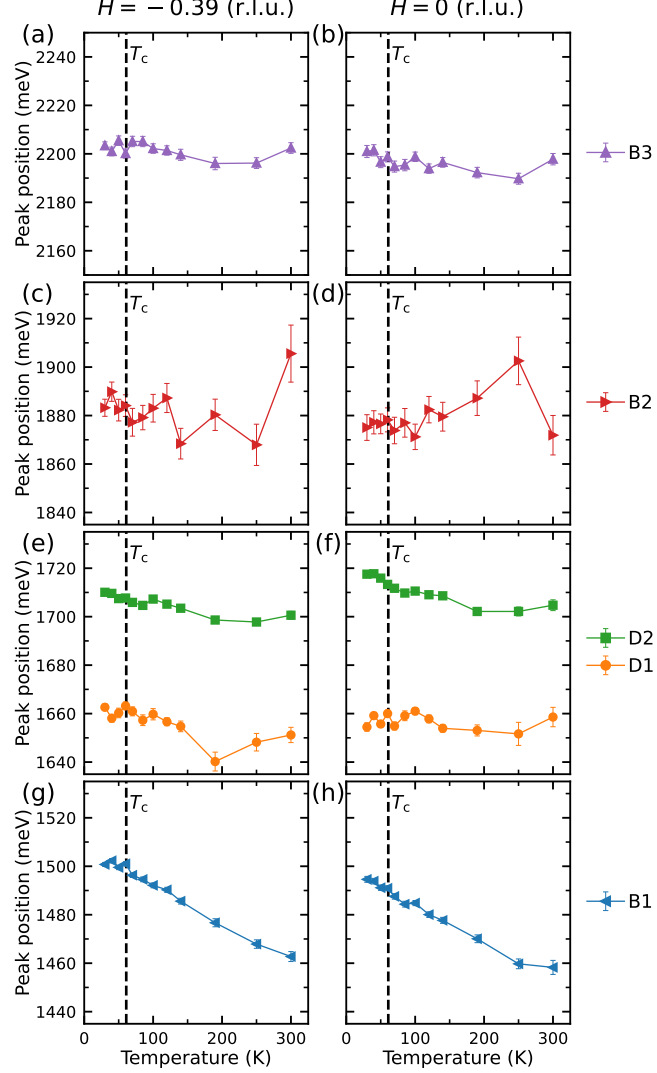


FIG. S12. The extracted temperature dependent energies of the excitons at two different in-plane momenta ( $H = -0.39$  and  $H = 0$  r.l.u.). Error bars represent one standard deviation. The dashed lines indicate the FM transition temperature  $T_c$ .

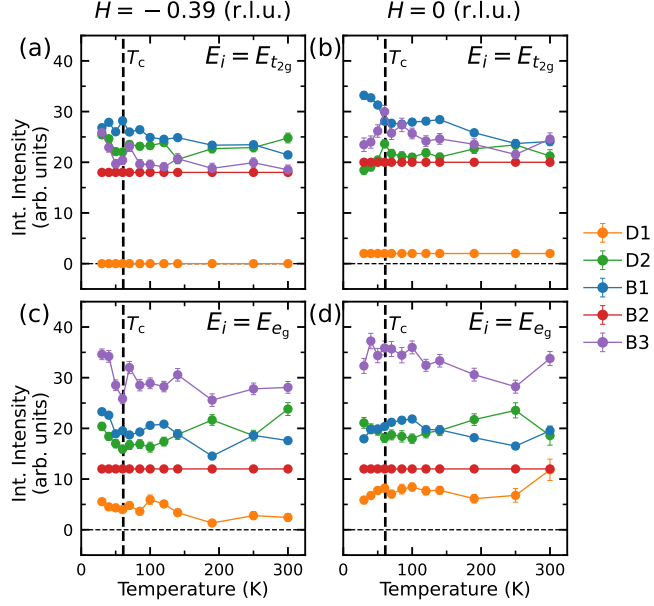


FIG. S13. Temperature dependence of the dark excitons at (a),(c)  $H = -0.39$  r.l.u. and (b),(d)  $H = 0$  at two different in-plane momenta ( $H = -0.39$  and  $H = 0$  r.l.u.). This re-plots the same data as in Fig. 3 of the main text and Fig. S3, but using integrated intensity rather than peak height. Error bars represent one standard deviation.

#### S4. INTEGRATED PEAK INTENSITY TEMPERATURE DEPENDENCE

For completeness, here in Fig. S13 we re-plot the same data provided in Fig. 3 of the main text and Fig. S3 in terms of integrated peak intensity rather than peak height. The anomalies across  $T_c$  are apparent in integrated peak intensity as well. This is because of the slow change in peak width below  $T_c$ . Note that the integrated intensity of B2 at both resonance energies and D1 at the  $E_{t_{2g}}$  resonance are fixed in the whole temperature range as explained in Sec. S3 D.

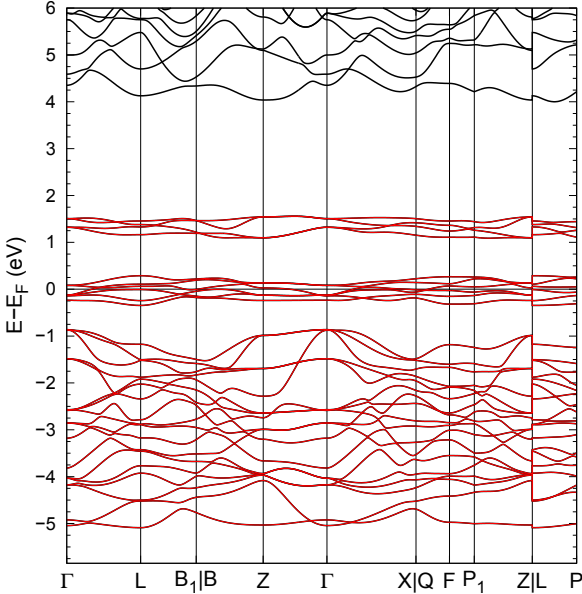


FIG. S14. Band structure of  $\text{CrI}_3$  without spin-orbit coupling. Wannier projected bands are in red, overlaid on the DFT calculated bands in black showing their agreement.

TABLE S1. Full list of parameters used in the single site atomic model calculations.  $F_{dd,i}$  and  $F_{dd,n}$  are for the initial and intermediate states, respectively. Units are eV.

$10D_q$	$F_{dd,i}^2$	$F_{dd,i}^4$	$F_{dd,n}^2$	$F_{dd,n}^4$	$F_{dp}^2$	$G_{dp}^1$	$G_{dp}^3$	$\zeta_i$	$\zeta_n$	$\zeta_c$
1.50	6.574	4.121	7.074	4.435	3.067	2.250	1.279	0.035	0.047	5.667

## S5. FURTHER DETAILS OF ED RIXS CALCULATIONS

To verify the suitability of the hopping matrix in the main text, we overlay the Wannier projected bands with the original density functional theory (DFT) in Fig. S14. We also provide further details of our atomic model for  $\text{CrI}_3$  and the spin and angular dependence of the spectra.

### A. Single site atomic model

We also tested a simpler model that only considers a single  $\text{Cr}^{3+}$  ion with 10 effective  $3d$  orbitals. In this case, only three independent parameters are used, including  $k_{dd}$ ,  $k_{dp}$  and  $10D_q$ . Again,  $k_{dd}$  dictates the energies of the dark excitons D1 and D2, and  $k_{dp}$  affects the resonance profiles of the excitations. Therefore, their refined values ( $k_{dd} = 0.61$ ,  $k_{dp} = 0.47$ ) are very close to that in the Anderson impurity model (AIM). However, the energy of exciton B1 is exclusively governed by  $10D_q$ , which gives  $10D_q = 1.5$  eV. However, this choice of  $10D_q$  limits the energy of exciton B2 to  $\sim 2.3$  eV, much higher than the experimental value of 1.88 eV. Therefore, without explicitly including the ligand orbitals, we could not simultaneously obtain the correct energies for both B1 and B2. A comparison between the two models is displayed in Fig. S15, with the full parameters presented in Tab. S1. The failure of the atomic model further underlines the fact that  $\text{CrI}_3$  is a self-doped charge transfer material.

### B. XAS state analysis

We use  $E_{t_{2g}}$  and  $E_{e_g}$  to label the resonance energies at  $E_i = 575.1$  eV and 576.3 eV. To support this assignment, we calculated the relevant quantum numbers for the intermediate state in the atomic model approximation, which captures the resonance behavior reasonably well as shown in Fig. S15. The result is presented in Fig. S16. As expected, there is strong mixing between  $t_{2g}$  and  $e_g$  orbitals, however, a substantial change in  $t_{2g}$  vs.  $e_g$  is seen, confirming that

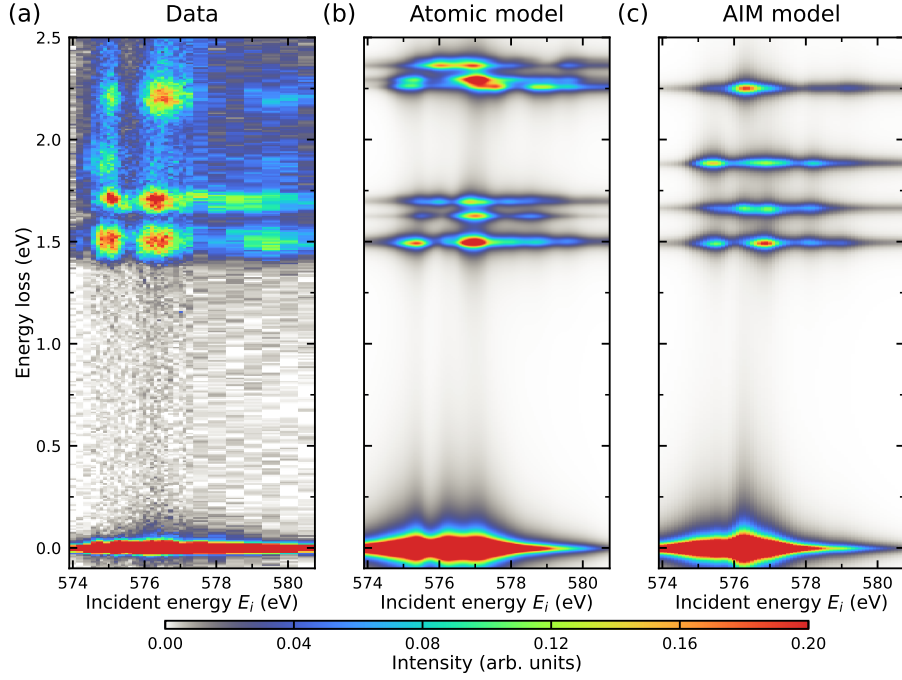


FIG. S15. Comparison of RIXS energy maps calculated using different models. (a) The measured RIXS energy map. (b) The calculated RIXS energy map using an atomic model. (c) The calculated RIXS energy map using an AIM. Panels (a),(c) use the same data shown in Fig. 4(a)–(b) and are replotted here for comparison.

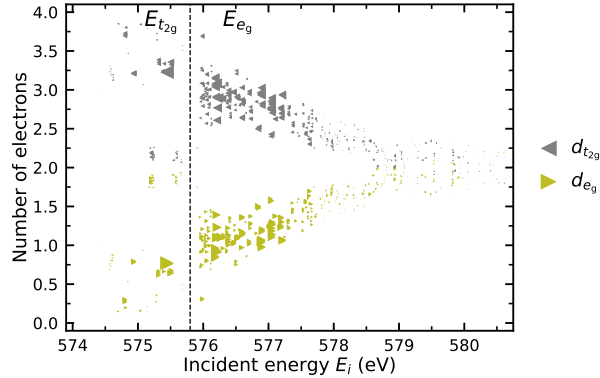


FIG. S16. Electron occupations of  $t_{2g}$  and  $e_g$  orbitals in the intermediate state of the atomic model. The symbol size (area) is proportional to the calculated intensity of each state.

our labels are reasonable.

### C. Angular dependence

In the measured in-plane momentum dependence of the RIXS spectra, we observe that the intensity of the D1 exciton reaches its maximum near the Brillouin zone center at  $E_{t_{2g}}$  resonance. This trend is qualitatively captured by the angular dependence of the calculated RIXS spectra. In Fig. S17, we show the calculated intensity of this exciton D1 as a function of the incident angle  $\theta$  at  $E_{t_{2g}}$  resonance using the AIM. By varying the incident angle, we essentially change the polarization of the incident and scattered photons, which ultimately affects the RIXS cross section.

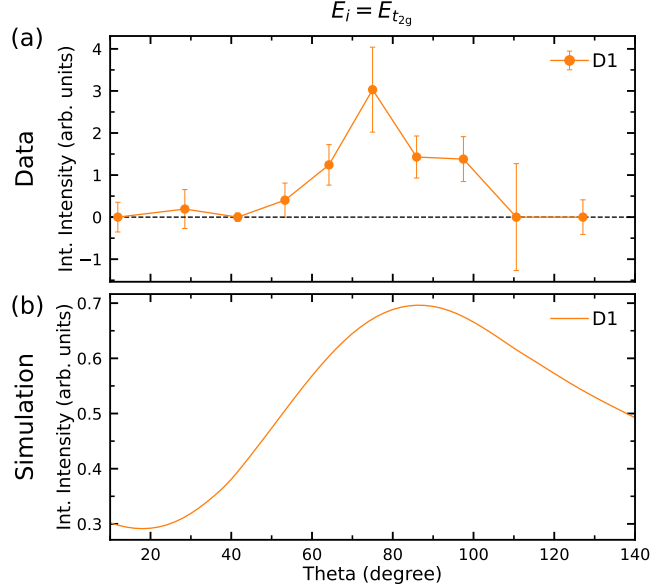


FIG. S17. Comparison between the measured and calculated incident-angle theta dependent dark exciton D1 intensity at  $E_{t_{2g}}$  resonance. The calculation is based on the AIM. The calculation nicely reproduces the trend of the intensity.

#### D. Spin direction dependence

We have shown an abrupt change in the dark exciton intensity across the FM transition temperature  $T_c$ . Here, we examine one possible origin by considering the spin-direction dependent RIXS spectra. The rationale is that the spin direction, which is clearly different across  $T_c$ , can potentially affect the RIXS cross section. Below  $T_c$ , CrI<sub>3</sub> is in the FM state with spins pointing along *c*-axis, whereas above  $T_c$ , it enters the paramagnetic state with randomly oriented spins. This change in spin direction can be simulated by controlling the direction of the external magnetic field **B** in the Zeeman term. The representative calculated spectra based on the AIM are shown in Fig. S18. The calculated dark exciton intensity barely changes in comparison to the bright excitons, contrary to the trends observed from the experimental spectra. Thus, the peculiar temperature dependence cannot be simply explained by the spin-direction dependence and likely requires more complicated explanations involving exciton-magnon interactions.

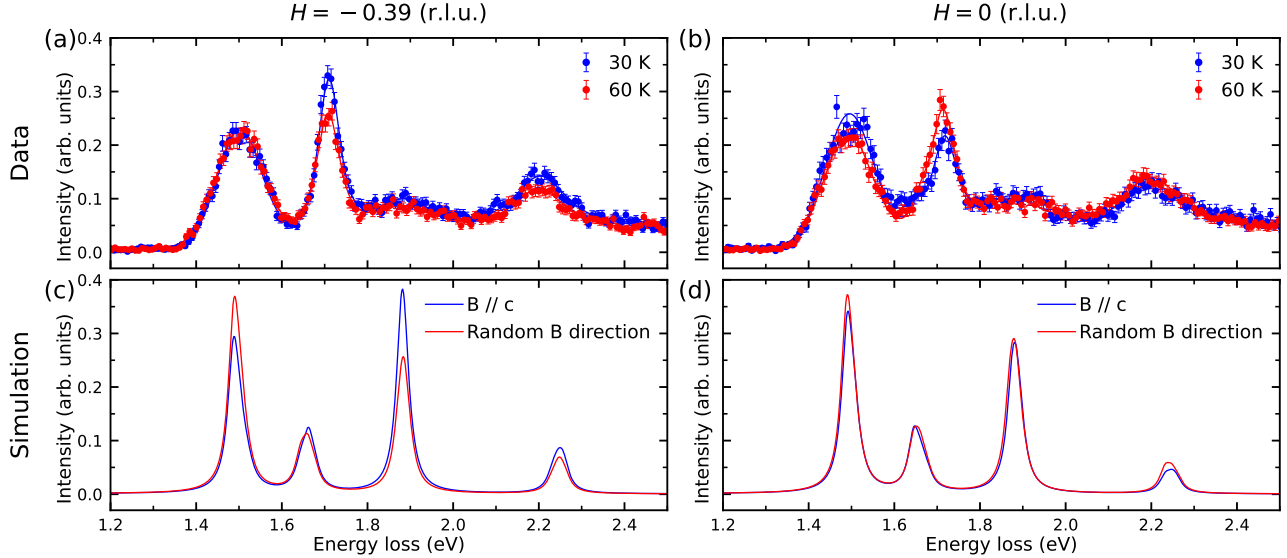


FIG. S18. Comparison between the measured and calculated RIXS spectra. (a),(b) Representative measured RIXS spectra at two different momentum transfers at two temperatures. The solid lines are the fits to the data. Blue data is within the magnetically ordered phase well below the FM transition temperature  $T_c$ , whereas red data is near  $T_c$  with much reduced ordered moment. (c),(d) Corresponding calculated RIXS spectra based on the AIM to simulate the spin direction effect. The blue lines assume the spin directions are aligned along the  $c$ -axis, while the red lines assume random spin directions. The calculations predict negligible changes in the intensities of the dark excitons, in contrast to the experimental observations.

## S6. AN ASIDE ON TERMINOLOGY

Here, we further discuss whether the excitations in  $\text{CrI}_3$  should be classified as  $dd$ -excitations or, more generally, as excitons. This requires a precise definition of  $dd$ -excitations. The strictest definition involves transitions that, to a good approximation, occur only within local  $d$ -orbitals. A broader but still rigorous definition describes  $dd$ -excitations as transitions within an effective manifold of hybridized  $d$ -orbitals centered on the transition metal site in an atomic-like model. Based on either definition, it is clear that  $\text{CrI}_3$  does not host strictly defined  $dd$ -excitations (see Fig. 4 of the main text and Sec. S5 A).

However, less stringent definitions of  $dd$ -excitations are sometimes employed in the literature. The term  $dd$ -excitation is generally less likely to be used for a transition that exhibits interesting coupling to magnetism, but there are exceptions here. The terms exciton and  $dd$ -excitation are also sometimes associated with narrow and broad linewidths, respectively, but to our knowledge, no attempt has been made to quantify the boundary between these categories. Furthermore, as linewidths depend on material purity and temperature, such distinctions are not necessarily meaningful. The overwhelming majority of papers consider  $dd$ -excitation local transitions not dispersive quasiparticles.

Our newly discovered 1.7 eV transitions in  $\text{CrI}_3$  are dispersive, exhibit temperature dependence across the magnetic transition, and display narrow linewidths both in general and compared to other transitions in the material. All these properties are more compatible with the use of the term exciton than the typical use of the term  $dd$ -excitation. Despite the partial ambiguity, we conclude that D1 and D2 are best termed excitons.

